Journal of Materials Chemistry

Cite this: J. Mater. Chem., 2012, 22, 14205

www.rsc.org/materials

PAPER

Nanostructured homogenous CdSe–TiO_2 composite visible light photoanodes fabricated by oblique angle codeposition†

George K. Larsen,*[a] Bob C. Fitzmorris,[b] Claudia Longo,[c] Jin Z. Zhang[b] and Yiping Zhao[a]

Received 23rd April 2012, Accepted 5th June 2012
DOI: 10.1039/c2jm32551a

A unique fabrication method, oblique angle codeposition, is used to deposit well-aligned nanorod arrays and thick films of homogenously mixed CdSe–TiO_2 composites. The composite films are characterized structurally, optically, and photoelectrochemically using a variety of experimental techniques. The CdSe–TiO_2 composites are compared with pure CdSe and TiO_2 films in order to determine their utility for photoelectrochemical (PEC) applications and to understand the mechanisms underlying the observed behaviors. The evaporation process of CdSe creates three different cluster types within the TiO_2 film structures: isolated Se, Se-deficient CdSe, and Se-rich CdSe. The prevalence of each cluster type is dependent on predicted film composition, and each is affected differently by open-air annealing. Isolated Se can be incorporated into the TiO_2 lattice, resulting in low energy rutile phase. Se-deficient CdSe clusters crystallize preferentially into cubic CdSe and are easily oxidized into CdO, while Se-rich CdSe clusters crystallize into hexagonal CdSe and are more stable. Furthermore, each of these cluster types interacts differently with the surrounding TiO_2 matrix, resulting in diverse optical and PEC behaviors. Importantly, the composite nanorod structure is a more efficient photoanode under visible light illumination than both the pure CdSe and TiO_2 nanorod array films. The stoichiometry of the CdSe domains is more important than overall CdSe content within the film in determining the structural, optical, and PEC properties of the films.

1. Introduction

The development of a clean, viable, sustainable, and widely available energy resource is, perhaps, the greatest challenge of the twenty first century. The sun is a particularly attractive source of energy since it fits these criteria quite well and is the progenitor, in some manner, of all other energy resources on the planet. Therefore, there has been a tremendous amount of research recently which focuses on improving solar energy conversion efficiency. Solar energy is often converted into electrical energy using solar cells, but it also can be converted into chemical energy in the form of hydrogen. This can be done using a semiconductor as a photoanode in a photoelectrochemical (PEC) cell.[1,2] In a PEC device, photogenerated electrons in the semiconductor photoanode are transferred through an external circuit to the cathode, which generate hydrogen from protons. The holes left behind oxidize water to generate oxygen and protons. One advantage of converting solar energy into hydrogen fuel is that locations of energy production and energy consumption can by spatially and temporally separated. Nanostructured titanium dioxide (TiO_2) has been the focus of water splitting research because TiO_2 is abundant, inexpensive, nontoxic, and has a band gap that spans both the hydrogen and oxygen evolution potentials in water. Nanostructuring TiO_2, in addition to other advantages, creates a large surface-to-volume ratio which leads to enhanced efficiency.[3–5] However, the practical efficiency of nanostructured TiO_2 for direct solar energy conversion is limited because of its weak absorption in the visible region of the spectrum due to its large band gap. Therefore, much research has been devoted to extending the photoresponse of TiO_2 into the visible region to encompass more of the solar spectrum. Doping foreign elements into TiO_2 to create donor or acceptor levels within the band gap is a common method of extending the photoresponse into the visible region.[6–8] A more intriguing method couples smaller band gap materials with TiO_2.[9–11] Upon visible light photoexcitation, the smaller band gap material can transfer charge carriers to TiO_2 if it is energetically favorable. Thus, if the valence band edge of the sensitizing material is lower than the valence band edge of TiO_2,

[a]*Department of Physics and Astronomy, and Nanoscale Science and Engineering Center, University of Georgia, Athens, Georgia 30602, USA. E-mail: georgelarsen@physast.uga.edu; Fax: +1 (706) 542-2492; Tel: +1 (706) 542-6230*
[b]*Department of Chemistry and Biochemistry, University of California, Santa Cruz, California 95064, USA*
[c]*Institute of Chemistry, University of Campinas – UNICAMP, P.O. Box 6154, 13084-971 Campinas, SP, Brasil*

† Electronic supplementary information (ESI) available: SEM images, XRD and Raman spectra of annealed TiO_2 films; photograph of as-deposited and annealed films; Gaussian deconvolution of IPCE spectra. See DOI: 10.1039/c2jm32551a

a hole can transfer from the smaller band gap material into the valence band of TiO_2. Similarly, if the conduction band edge of the sensitizing material is higher than the conduction band edge of TiO_2, electrons can transfer from the smaller band gap material into the conduction band of TiO_2. Coupling TiO_2 with an appropriate smaller band gap material offers a promising route to increasing PEC efficiency because it not only extends the photoresponse into the visible region, but it also enhances charge separation, which increases the chances of the free charge being utilized in reduction or oxidation reactions. Cadmium selenide (CdSe) has been shown to be an interesting sensitizer for TiO_2 because of its ability to transfer photoexcited electrons into the TiO_2 conduction band and the known tunable quantum size effects of CdSe quantum dots.[12–15] Most studies in the literature have utilized wet chemistry to fabricate nanostructured CdSe–TiO_2 coupled films.[16–20] Typically, these studies report on CdSe–TiO_2 architectures where CdSe quantum dots are molecularly linked to the surface of TiO_2. While most of these studies have been successful in creating relatively efficient solar energy conversion devices, there are some drawbacks to wet chemical synthesis: the structural design of such devices is limited; molecular linkers complicate charge transfer across interfaces;[21–23] and different materials are synthesized using different methods, making analysis across different architectures and material compositions difficult.

Very recently, we have demonstrated that, by using an oblique angle codeposition technique, well-aligned nanocomposite or doped nanorod arrays can be fabricated.[24–28] Oblique angle codeposition is a physical vapor deposition (PVD) method which combines codeposition and the oblique angle deposition (OAD) technique. OAD is a well known PVD technique where the vapor incident direction and the substrate normal form a large angle, and arrays of well-aligned tilted nanorods develop spontaneously due to the shadowing effect of previously deposited material.[29,30] Codeposition refers to the simultaneous evaporation of two or more materials to form composite materials, where the composition of the resulting nanostructures can be controlled by varying the relative ratio of deposition rates of the source materials. Thus, oblique angle deposition combined with codeposition is a flexible fabrication method that can synthesize precisely designed nanostructures of densely coupled composites of varying material composition.

In this study, we use the codeposition method to fabricate both OAD nanorod arrays and thick films of homogenously mixed CdSe–TiO_2 composites with various material compositions, which are compared with both pure CdSe and pure TiO_2 films fabricated using a single source deposition. The homogenous mixture of both materials within the CdSe–TiO_2 nanorod and thick film structures without molecular linkers creates an environment which is favorable for efficient charge transfer. Indeed, our companion paper,[31] which reports on the ultrafast charge dynamics of the OAD CdSe–TiO_2 composite films, reveals that these structures have among the highest electron injection rates from CdSe into TiO_2. The very fast injection rate is attributed to the large interfacial area and strong electronic coupling between the two materials. Given these results, it is expected that the OAD CdSe–TiO_2 composites should be promising materials for solar energy conversion. In this paper, the structural, optical, and PEC properties of CdSe–TiO_2 films fabricated by oblique angle codeposition are investigated in detail and compared with pure CdSe and pure TiO_2 films in order to assess the utility of CdSe–TiO_2 composites for PEC applications and to understand the mechanisms governing the observed behaviors. We find that the composite nanorod structure can be a more efficient visible light photoanode than both the pure CdSe and TiO_2 films. Furthermore, the stoichiometry of the CdSe domains is found to be more important than overall CdSe content within the film in determining the structural, optical, and PEC properties of the films.

2. Experimental methods

Both CdSe–TiO_2 composite nanorod arrays (OAD) and thick films were deposited using electron beam codeposition. The CdSe–TiO_2 composite films and the pure CdSe and TiO_2 films were fabricated by a unique, custom designed vacuum deposition system equipped with two electron-beam evaporation sources (Pascal Technology).[32] The source materials used were TiO_2 (99.9%, Kurt J. Lesker) and CdSe (99.995%, Alfa Aesar). No other gases were introduced into the chamber during depositions. Prior to the deposition, the vacuum chamber was evacuated to a pressure of 1×10^{-6} Torr, and the background pressure during the deposition was maintained at less than 5×10^{-6} Torr. Precleaned glass microscope slides, Si wafers, and indium tin oxide (ITO) coated glass slides were used as substrates, and were chosen for different characterizations. The substrate normal was positioned at 0° from the vapor incident direction for the thick film depositions and at 86° for the OAD depositions. The CdSe/TiO_2 ratio was controlled by the relative growth rates of CdSe and TiO_2, which were monitored independently by two separate quartz crystal microbalances (QCMs), where each QCM only faces the corresponding vapor flux direction. The relative growth rates and corresponding predicted compositions are listed in Table 1. To simplify the notation, we denote the composite samples as C^mT^n, where C represents CdSe, T represents TiO_2, and m and n represent the molecular percentages (mol%) of CdSe and TiO_2, respectively. For the OAD films, the materials were deposited onto the substrates until the combined QCM readings totaled 1.5 μm. For the thick films, excluding the $C^{33}T^{67}$ film, the materials were deposited onto the substrates until the combined QCM readings totaled 1 μm. For the $C^{33}T^{67}$ film, material was deposited until the combined QCM reading totaled 1.5 μm. After the depositions, half of the films were randomly chosen to be annealed in open air in a quartz tube furnace (Lindberg/Blue M Company) for 5 hours at annealing temperature $T = 400$ °C.

The nanorod arrays and thick films were characterized by different sets of experimental techniques since a specific film structure makes certain techniques more relevant and appropriate. The structure and morphology of the OAD films were characterized by a field-emission scanning electron microscope (SEM) equipped with energy dispersive X-ray spectroscopy (EDX) (FEI Inspect F). The EDX spectra of the thick films were measured using the EDX equipped SEM at 20 kV accelerating voltage. X-ray diffraction (XRD) data were collected for both the OAD and thick films on a PANalytical X'Pert PRO using a Cu-Kα radiation source ($\lambda = 1.5418$ Å). Raman spectra of the OAD films were acquired using a Bruker SENTERRA confocal Raman microscope system through a 50× objective with a laser excitation wavelength of 532 nm, power of 10 mW, and

Table 1 Compositional parameters of the CdSe–TiO_2 composite films

Film	TiO_2 rate (Å s^{-1})	CdSe rate (Å s^{-1})	Predicted CdSe (mol%)	Measured CdSe: as-deposited (mol%)	Measured CdSe: $T = 400$ °C (mol%)
TiO_2	4	—	—	—	—
$C^{13}T^{87}$	4	1.05	13	8.1 ± 0.9	7.7 ± 0.5
$C^{23}T^{77}$	4	2.09	23	19.6 ± 0.7	21 ± 2
$C^{33}T^{67}$	4	3.49	33	33 ± 2	34 ± 2
$C^{40}T^{60}$	4	4.8	40	44 ± 7	40 ± 3
$C^{46}T^{54}$	3	4.44	46	43 ± 2	42 ± 2
CdSe	—	4	—	—	—

a collection time of 60 seconds. The optical absorbance spectra of the OAD films were measured by a double beam UV-Vis-NIR spectrophotometer (JASCO V-570).

Photoelectrochemical measurements of the OAD films were performed as follows. A 1000 W Xe lamp (Oriel Research Arc Lamp assembly #69924 and power supply #69920) was utilized as a white light source, an infrared (IR) water lamp filter was then attached (Oriel # 6127), and the white light beam was coupled to a monochromator (Oriel Cornerstone 130 1/8m) for spectral resolution from 300 to 800 nm. Irradiance measurements were performed with a Kettering (#68) and Coherent Field Mate power meter with overall white light intensity of 100 mW cm^{-2}. PEC photoanodes were created by first securing a copper wire to a bare portion of the ITO substrate with high purity silver paint. The cells were then sealed on all edges and upon the active area (OAD or OACD nanorod arrays) with epoxy resin except for a working electrode surface area of around 0.5 cm^2 (the exact area of each electrode was measured individually). The electrolyte solution used in all experiments was 0.25 M Na_2S and 0.35 M Na_2SO_3 at a pH of 9.5. Reference and counter electrodes during the PEC measurements were a Ag/AgCl electrode (CHI Instruments/1 M KCl) and a coiled Pt electrode, respectively. The photoanode cyclic voltammograms were measured by sweeping from a potential of −1 to 0.2 V *vs.* the reference. Photocurrent was measured at 10 nm intervals from 280 nm to 750 nm at a potential of −0.35 V *vs.* the reference and the current under white light and in the dark were also measured at the same potential.

3. Results and discussion

3.1 Structural properties of CdSe–TiO_2 films

3.1.1 Composition. The actual material compositions of the composite and pure films were confirmed by EDX measurements of the thick films. EDX analysis of the OAD films was not considered due to their large porosity and small material volume, which makes accurate measurement difficult. As shown in Fig. 1, all films containing CdSe show an excess of Se in the spectra. The ratio of Se to Cd is not constant. Films with the smallest CdSe content have the greatest imbalance, with the Se/Cd ratio reaching as high as 2.1 in the $C^{28}T^{72}$ film and decreasing to 1.2 in the pure CdSe film. After annealing, the measured Se/Cd ratios remain mostly unchanged. There is some indication that for composite films with higher CdSe content that there could be some Se loss through vaporization during the annealing process, but this loss, if it occurs, is minimal and falls within the experimental error. Similar to the as-deposited CdSe, the as-deposited TiO_2 is

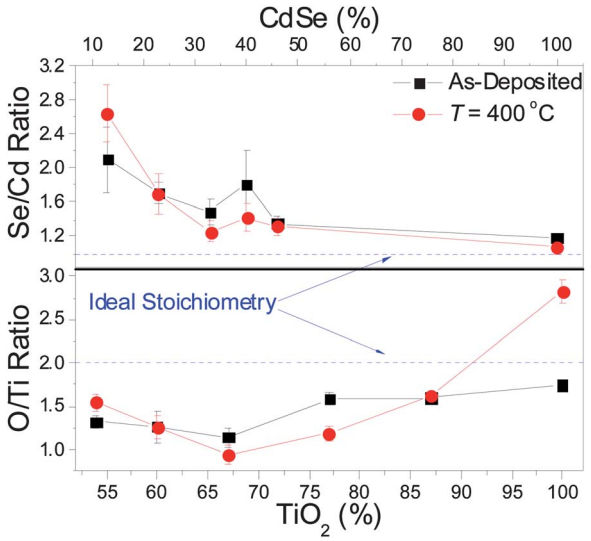

Fig. 1 EDX measured Se/Cd ratio *versus* CdSe content and O/Ti ratio *versus* TiO_2 content.

generally non-stoichiometric, and the stoichiometry of the TiO_2 improves as it increases in relative percentage of the material. The largest measured O/Ti ratio occurs for the pure TiO_2 film at 1.7, and the lowest occurs for the $C^{33}T^{67}$ film at 1.1. After annealing at $T = 400$ °C, the O/Ti ratio either decreases slightly or remains the same in the composite films. In the pure TiO_2 film, the O/Ti ratio exceeds the ideal stoichiometry value of 2 after annealing.

The actual CdSe molecular percentage (mol%) of each composite film is calculated by (Cd + Se)/(Cd + Se + Ti + O), using EDX measured atomic percentages, as shown in Table 1. Despite the non-stoichiometry of the deposited materials, the CdSe molecular percentages of the films are mostly similar to the predicted values. The $C^{13}T^{87}$ film exhibits the greatest deviation from the expected value, with 8.1 mol% measured *versus* 13 mol% expected. The change in the CdSe mol% after annealing at $T =$ 400 °C is slight and correlated with the change in the Se/Cd ratio described above. Note that in this report all films will continue to be referred to by the predicted material composition unless it is noted otherwise.

This composition dependence of the stoichiometry of CdSe in the films can be explained by the sublimation behavior of CdSe. Sigai and Wiedemeier have shown that the sublimation of CdSe is a two phase process.[33] The initial phase occurs at 450 °C and is characterized by the vaporization of Se only. After the Se/Cd ratio reaches 0.995–0.987, the selenium vaporization ceases. Increasing the temperature to 600 °C results in the next phase of CdSe sublimation, which is characterized by the congruent vaporization of both Cd and Se from the remaining Se-deficient CdSe solid. These two phases are described by the following reactions:

$$\mathrm{CdSe(s)} \rightarrow \mathrm{CdSe_{1-x}(s)} + \frac{x}{2}\mathrm{Se_2(g)} \quad (1)$$

$$\mathrm{CdSe_{1-x}(s)} \rightarrow \mathrm{Cd(g)} + \frac{1-x}{2}\mathrm{Se_2(g)} \quad (2)$$

They also note that both reactions (1) and (2) will occur simultaneously when CdSe is heated rapidly to 600 °C and above.

Electron beam evaporation of randomly sized pieces of CdSe in a crucible will produce similar results as rapid thermal heating since heat transfer between neighboring pieces of CdSe is inefficient and the heating rate is particle size dependent.

Therefore, it is expected that CdSe vaporization occurs through both reactions (1) and (2) during the electron beam deposition of the films. As shown in Table 1, when the CdSe–TiO_2 composites were deposited, the deposition rate of TiO_2 was kept relatively constant, while the rate of CdSe was increased gradually with increasing CdSe composition. For films with the smallest CdSe composition, the lower power of the electron beam and the smaller total thickness of CdSe deposited favors a relatively large amount of Se vaporization occurring through reaction (1). Increasing the beam power and total thickness of CdSe deposited increases the amount of CdSe vaporization occurring through reaction (2) relative to the Se vaporization occurring through reaction (1). Thus, the stoichiometry of the CdSe improves with increasing CdSe composition.

The oxygen-deficient stoichiometry of the as-deposited TiO_2 is not surprising and is consistent with previous studies of electron beam evaporated TiO_2.[27,34] However, the observation that the measured O/Ti ratio of the composite films remains mostly unchanged with annealing is contrary to what is expected, as annealing at a high temperature in open air should passivate oxygen vacancies and increase the overall oxygen content in the films. This effect is clearly seen in the measured O/Ti values of the pure TiO_2 samples before and after annealing (Fig. 1).

3.1.2 OAD film morphology. Fig. 2 shows the representative SEM images of the pure and composite as-deposited and annealed films. As indicated by SEM, the large-scale morphology of the OAD films varies slightly with material composition. The pure films show more isolated nanorods, while in the composite films the nanorods are more densely packed especially in the direction that is perpendicular to the incident vapor flux. This bunching effect is more pronounced for the films with greater CdSe composition. Additionally, the SEM images of the as-deposited OAD films show that the morphological parameters of the individual nanorods vary for different material compositions. Table 2 summarizes the average nanorod length, tilting angle, and surface area. The average nanorod length in the pure TiO_2 film is 1.42 μm, and in the pure CdSe film it is 1.11 μm. In the composite OAD films, the nanorod length initially decreases with increasing CdSe composition, with the heights reaching as low as 0.85 μm for the $C^{33}T^{67}$ film, then increases monotonically for CdSe compositions greater than 33%. The tilting angle for most films are close to 55°, but increase to 59°, 66°, and 66° for the $C^{33}T^{67}$, $C^{40}T^{60}$, and $C^{46}T^{54}$ films, respectively. The nanostructured surface area to substrate ratio is calculated from the average surface area of the individual nanorods multiplied by the average nanorod density. The pure CdSe film shows the smallest surface area ratio at 8, and the longest, more densely packed composites, $C^{13}T^{87}$ and $C^{46}T^{54}$, have the highest ratios at 16.9 and 18, respectively. Most of the nanorod films show no obvious morphological changes after annealing. However, the morphology of the nanorods in the pure CdSe film changes dramatically after annealing, as the surface of annealed nanorods has a melted appearance (Fig. 2).

Table 2 Dimensional parameters of the CdSe–TiO_2 composite films

Film	Nanorod length (μm)	Tilting angle (°)	Surface area/ substrate area	Total deposition rate (Å s^{-1})
TiO_2	1.42 ± 0.03	55 ± 1	11.0 ± 0.5	4
$C^{13}T^{87}$	1.09 ± 0.03	54 ± 1	16.9 ± 0.5	5.05
$C^{23}T^{77}$	0.92 ± 0.04	53 ± 1	9.7 ± 0.3	6.09
$C^{33}T^{67}$	0.85 ± 0.04	59 ± 1	10.8 ± 0.2	7.49
$C^{40}T^{60}$	0.93 ± 0.05	66 ± 2	10.7 ± 0.4	8.8
$C^{46}T^{54}$	1.07 ± 0.03	66 ± 1	18 ± 3	7.44
CdSe[a]	1.11 ± 0.04	55 ± 4	8 ± 1	4

[a] For the as-deposited film only.

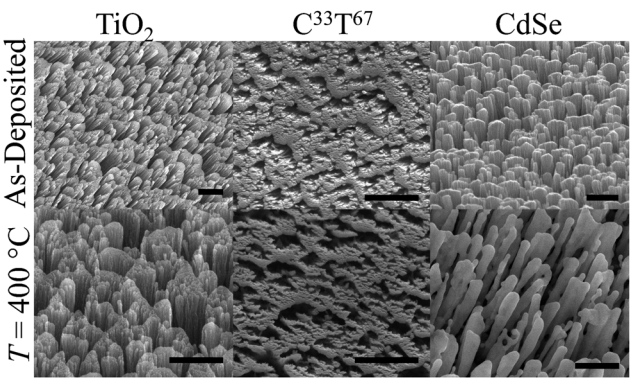

Fig. 2 SEM images of the pure TiO_2, $C^{33}T^{67}$, and pure CdSe films, before and after annealing at $T = 400$ °C for 5 hours. The scale bar in each image represents 500 nm (see ESI Fig. S1† for top view SEM images of all of the films).

The variation in nanorod length with CdSe composition is due to composition dependent material losses from scattering processes occurring during the codeposition. The variation of the tilting angle is interesting, as both the pure TiO_2 and the pure CdSe films have the same tilting angle. This indicates that the change in angle is the result of deposition parameters rather than the result of competing material properties as seen in other codeposited films.[35] Theoretical models of columnar growth show a decreasing tilting angle as the deposition rate increases.[36] This is contrary to what is seen in the CdSe–TiO_2 composite films where the nanorods show a tilting angle of ~55° for some films, but increase to larger angles for the films which had the highest deposition rates. Thus, it is clear that the change in tilting angle is related to the higher rates, but mechanism behind this relationship is unclear.

Interestingly, the pure CdSe nanorods appear to have melted after annealing at $T = 400$ °C. While the melting point of nanosized CdSe has been shown to reach as low as 550 °C for isolated 7 nm quantum dots,[37] this temperature is still greater than the annealing temperature of 400 °C, and the CdSe in the polycrystalline nanorods are expected to have a melting point closer to the bulk value of 1240 °C given the larger structure and grain size. Thus, the melting of CdSe is not the likely explanation for the melted appearance of the annealed pure CdSe film. These effects can be explained by the excess Se in the non-stoichiometric evaporated CdSe (Fig. 1). In the pure CdSe film the excess Se exists as elemental selenium, which has a melting point of 221 °C, and annealing at $T = 400$ °C causes this pure selenium to melt. The melting Se destabilizes the nanorod structure and gives

the pure CdSe nanorod film its melted appearance. In the composite films, the measured value of Se/Cd is greater than in the pure CdSe film, but the total amount of excess Se is much lower since the Se and CdSe are guests within the TiO_2 host material. Therefore, the melting effect, if it occurs, will be less pronounced and may not be perceptible. Additionally, the as-deposited TiO_2 is oxygen-deficient, and the excess Se can incorporate itself into the TiO_2 lattice *via* oxygen vacancies. This process is energetically favorable, as it has been shown using density functional theory, that for Se atoms in an oxygen-deficient TiO_2 lattice, it is energetically more favorable for the Se to reside at substitutional sites than at interstitial sites.[38] The excess Se in the composite films that becomes incorporated into the TiO_2 is not expected to melt. Thus, the morphology of the composite nanorods does not change after annealing.

3.1.3 XRD characterization. XRD spectra of the CdSe–TiO_2 films were taken in order to confirm the crystalline properties of the films (Fig. 3). For the as-deposited thick films, the XRD spectra showed no evidence of any crystal phase of TiO_2. However, the extremely broad peaks in the as-deposited composite thick films with CdSe composition greater than 23% are consistent with XRD patterns of both amorphous Se and amorphous CdSe.[39–41] The spectrum of the as-deposited pure CdSe thick film has peaks at $2\theta = 25°$, 41°, 45°, 49°, 52°, 63°, 71° which correspond respectively with the (002), (110), (103), (004), (112), (203), (105) crystal planes of hexagonal CdSe. No isolated peaks corresponding with the cubic phase of CdSe, Se, or Se_xO_y are seen in the thick film spectrum. The intensity of the strong peak at $2\theta = 25°$ in the thick film is due to the preferential crystallite orientation such that the *c*-axis is orthogonal to the plane of the substrate. Preferential crystal alignment in electron beam deposited CdSe thick films has been observed before.[42]

After annealing at $T = 400$ °C for 5 hours, the pure TiO_2 thick film shows the characteristic diffraction pattern of polycrystalline anatase TiO_2 (Fig. S2a†). The XRD spectrum of the pure CdSe thick film remains mostly unchanged after annealing, except for the two small peaks that appear at $2\theta = 30.5°$ and $2\theta = 69°$ in the diffraction pattern (Fig. 3a), which are related to the thermal oxide of CdSe. The XRD spectra of the composite thick films annealed at $T = 400$ °C do show sharp peaks, and this pattern varies for different CdSe compositions. The variation of

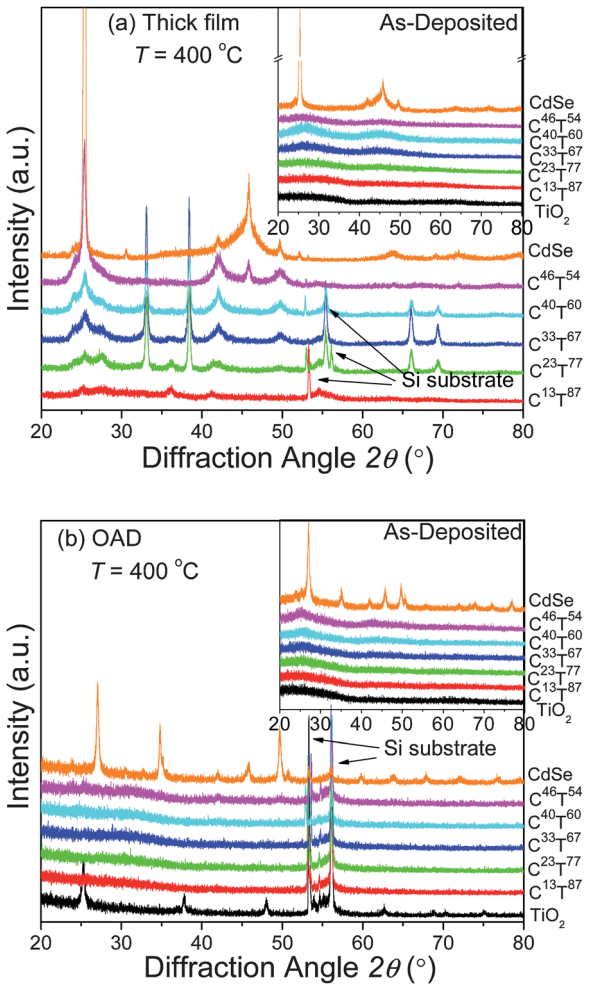

Fig. 3 XRD spectra of the (a) thick film and (b) OAD CdSe–TiO_2 composites annealed at $T = 400$ °C. The insets show the as-deposited spectra. Note that the spectra have been shifted vertically and the spectrum of the annealed pure TiO_2 thick film has been left out to improve clarity (see Fig. S2a†).

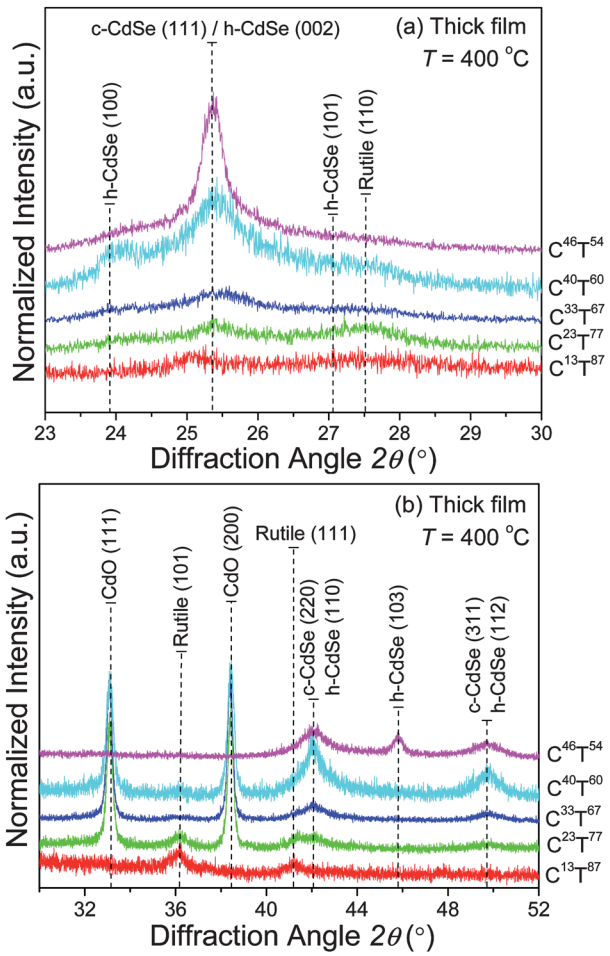

Fig. 4 XRD spectra of the CdSe–TiO_2 composite thick films annealed at $T = 400$ °C with peak attributions from (a) $2\theta = 23–30°$ and (b) $2\theta = 31–52°$. Note that the spectra have been normalized and shifted vertically to improve clarity.

diffraction pattern with CdSe composition is not straightforward and is the result of contributions from four different crystal phases: cubic CdSe (c-CdSe), hexagonal (h-CdSe), CdO, and the rutile phase of TiO_2 (Fig. 4a and b).

For the as-deposited OAD films, only the diffraction pattern of the pure CdSe film exhibited sharp peaks (Fig. 3b inset). Similar to the composite thick films, there are two extremely broad peaks in the spectra of the OAD films with CdSe compositions greater than 33%, which could be attributed to amorphous Se or amorphous CdSe. The pure CdSe OAD sample showed peaks at $2\theta = 23°$, 25°, 27°, 35°, 41°, 45°, 49°, 50°, 55°, 63°, 66°, 67°, 71°, 76° corresponding respectively with the (100), (002), (101), (102), (110), (103), (112), (201), (202), (203), (210), (211), (105), (300) crystal planes of hexagonal CdSe. No isolated peaks corresponding with the cubic phase of CdSe, Se, or Se_xO_y are seen for the pure CdSe OAD film. In standard powder diffraction data of hexagonal CdSe, the (100), (002), and (101) reflections have approximately the same relative intensity. In the spectrum of the pure CdSe OAD film the (101) reflection is significantly more intense than the (002) and (100) reflections, which indicates that the polycrystalline nanorods exhibit preferential crystal growth with the *c*-axis aligned with the long axis of the nanorod.

After annealing at $T = 400$ °C for 5 hours, both the pure TiO_2 and CdSe OAD films exhibit sharp, well-defined peaks (Fig. 3b). The pure TiO_2 film exhibits an anatase polycrystalline diffraction pattern after the annealing treatment, which is consistent with our previous results.[27] The XRD spectrum of the pure CdSe film remains mostly unchanged after annealing except for the four small peaks at 30.5°, 33°, 35°, and 60° that appear in the diffraction pattern, which are attributed to the thermal oxide of CdSe. For all of the composite films, the two broad peaks seen in the as-deposited spectra are not seen in the annealed spectra. The annealed $C^{46}T^{54}$ film has very faint peaks at $2\theta = 24°$, 25°, 27°, 42°, and 49° corresponding respectively with the reflections of the (100), (002), (101), (110), and (112) crystal planes of hexagonal CdSe. The spectra of the other composite films are essentially flat, and the only discernible peaks correspond with the Si substrate.

The XRD results of the pure OAD films and pure thick films are similar. Both of the pure TiO_2 films are amorphous as-deposited and crystallize into anatase after annealing. Both of the as-deposited pure CdSe films show preferentially oriented hexagonal crystallites, and, although the orientations of the crystallites in the OAD and thick films are different relative to the substrate, the orientations are similar in that the *c*-axis is preferentially aligned with the direction of material growth. After annealing, both pure CdSe films show evidence of thermal oxide formation. In previous reports, peaks attributed here to thermal oxide, have been attributed to CdO and $CdTiO_3$ in CdSe–TiO_2 composites[43] and to SeO_3 in chemically deposited CdSe.[44] However, in our films these peaks are related to the thermal oxide on CdSe. Using angle-resolved X-ray photoelectron spectroscopy, Masson *et al.* have determined that for polycrystalline CdSe annealed in dry air at 350 °C, the CdSe thermal oxide consists of a surface layer of SeO_x residing above deeper layers of CdO.[45] While the diffraction peaks in the measured spectra do not coincide perfectly with previously measured CdO or SeO_x patterns, the measured peaks at 30.5° and 35° are close to the (211) and (002) crystal plane reflections of SeO_2, which respectively appear at 29.7° and 35.4° and are the most intense peaks in the powder diffraction pattern of SeO_2. Thus, the oxidation peaks in the XRD spectra of the pure CdSe OAD and thick films are most likely related to the surface SeO_x species. The relative heights of the SeO_x diffraction peaks compared with the hexagonal CdSe diffraction peaks in the OAD and thick films indicate that the oxidation of CdSe is more significant in the OAD films, which is consistent with the higher surface area to volume ratio of these films.

For the composite films, it is expected that the phases present in the as-deposited OAD and thick films of the same composition should be very similar, and this is confirmed by the similarity of the XRD patterns for both sets of as-deposited films. After annealing, the XRD spectra of the different film structures are no longer similar; the thick films have well-defined diffraction patterns which vary with composition, while most of the OAD composite films show no discernible pattern. It is possible that the phase transition processes induced by the annealing treatment in the OAD films may be different than the processes induced in the thick films because the OAD films are highly porous and surface effects such as segregation, oxygen diffusion, and Se vaporization may play a more important role in these films. It is also possible that the phase transition processes are similar for both film structures, but the smaller material volumes of the OAD films hinder the XRD measurement of the thermally induced phases. This possibility is supported by the fact that the both the $C^{46}T^{54}$ OAD and thin film exhibit a similar hexagonal CdSe diffraction pattern, although the OAD pattern is much more faint.

In the composite thick films, the observed material composition dependence of the diffraction patterns can be understood through the evaporation process described by reactions (1) and (2). In the as-deposited films, reaction (1) creates isolated Se regions within the TiO_2 matrix, and reaction (2) results in regions in the TiO_2 with Se-deficient CdSe clusters ($CdSe_{1-x}$), as illustrated in Fig. 5. Additionally, these regions can overlap, creating regions within the TiO_2 matrix with Se-rich CdSe clusters. Each of these regions results in different phases after the thermal annealing treatment, and the prevalence of each type of region

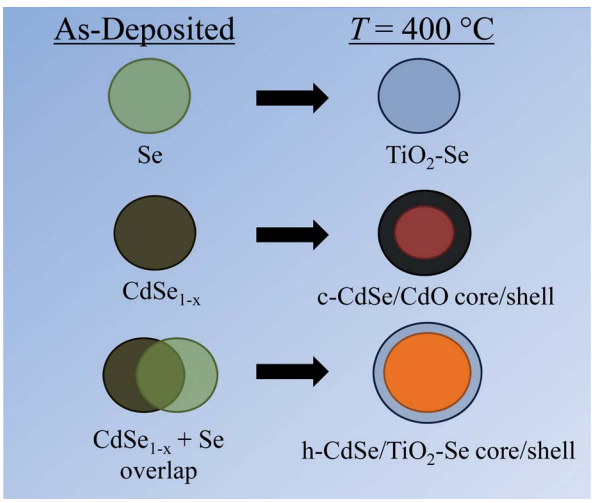

Fig. 5 Illustration of the proposed effect of the thermal annealing treatment at $T = 400$ °C on the as-deposited Se, $CdSe_{1-x}$, and overlap clusters residing in the TiO_2 matrix for the composite films.

and the corresponding overlap depend on the rate of CdSe evaporation and the total amount deposited, which leads to the CdSe composition dependence of the diffraction pattern. For the thick films with lower CdSe compositions, isolated Se regions will be more prevalent than the $CdSe_{1-x}$ clusters, as the composition of CdSe increases, the $CdSe_{1-x}$ cluster content increases relative to the isolated Se regions. However, as the total amount of CdSe evaporated increases, the likelihood that both $CdSe_{1-x}$ and Se regions overlap each other also increases. For the isolated Se regions, the Se can exist as elemental Se or be incorporated as an anion into the oxygen-deficient TiO_2 lattice (TiO_{2-x}) as described above, and this Se-doped region of TiO_2 crystallizes into the rutile phase (TiO_2-Se) when annealed at $T = 400$ °C. Typically, rutile crystallization occurs at a much higher temperature than 400 °C, so it is expected that the Se dopants reduce the thermal energy necessary for rutile transition to occur. A possible mechanism for this is the larger ionic radius of Se relative to O distorts the TiO_2 lattice and can force Ti into the interstitial regions. It has been proposed that the movement of Ti into interstitial spaces is a process that favors rutile formation.[46] Thus, there is an increasing presence of rutile in the XRD diffraction patterns with increasing excess Se and decreasing CdSe composition. This is in contrast to the pure TiO_2 thick film, which exhibits only an anatase pattern after annealing at $T =$ 400 °C. It has been demonstrated that the stoichiometry determines the phase manifestation of CdSe clusters, with Se-deficient CdSe preferring to crystallize in the cubic phase (c-CdSe) and Cd-deficient CdSe preferring the hexagonal phase (h-CdSe).[47] Therefore, it is proposed for the composite thick films that the Se-deficient CdSe clusters in the TiO_2 matrix crystallize into c-CdSe, while the CdSe clusters in the Se-rich overlap regions crystallize into h-CdSe. Although the Se/Cd ratio increases for decreasing CdSe composition, the Se-rich overlap regions are less likely to occur as the composition of CdSe decreases, so there is a decreasing presence of h-CdSe relative to c-CdSe with decreasing CdSe composition. The CdO diffraction peaks are the result of a thermal oxide shell surrounding the c-CdSe clusters. This process would similar to the thermal oxide formation described by Masson *et al.*,[45] except that the SeO_x outer layer would not form since the c-CdSe cluster is Se-deficient and, additionally, cationic Se is unstable in an O-deficient TiO_2 lattice.[38] Furthermore, the oxidation of c-CdSe regions into CdO is expected to only occur in regions close enough to the surface that can be reached by inward diffusing oxygen since it is unlikely that the CdO can be formed from O scavenged from an O-deficient TiO_2 lattice. It is important to note that the above processes appear to be strongly stoichiometry-dependent. Although the CdSe compositions are very similar, the XRD diffraction pattern of the $C^{46}T^{54}$ thick film is very different than the pattern of the $C^{40}T^{60}$ thick film. The primary compositional difference between the two films is that the $C^{40}T^{60}$ film is much more non-stoichiometric with respect to the CdSe.

3.1.4 Raman characterization of OAD films. Raman spectroscopy measurements were taken of the OAD films in order to further characterize the structural properties of these films (Fig. 6). For the pure TiO_2 OAD film, the as-deposited film showed no distinct Raman shifts, and the annealed film showed an anatase pattern, which is consistent with previous results.[27]

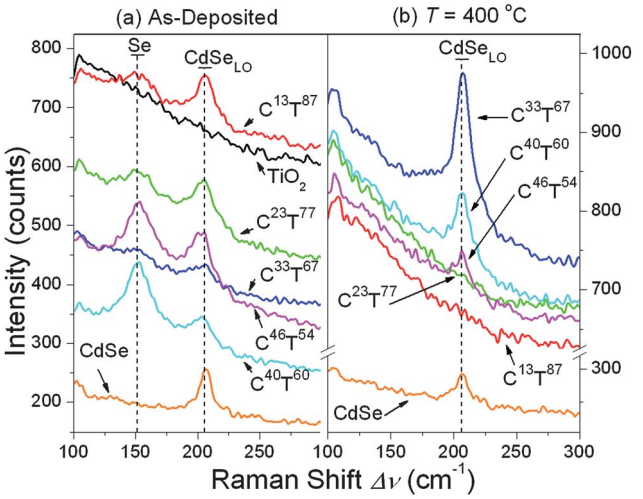

Fig. 6 Raman spectra with peak attributions of the as-deposited and annealed OAD films. Note that the spectrum of the annealed TiO_2 OAD film has been left out for clarity (see Fig. S2b†).

The Raman measurements show that all of the films intentionally doped with CdSe exhibit the characteristic Raman shift of the CdSe longitudinal optical phonon ($CdSe_{LO}$) at $\Delta\nu \approx 207$ cm^{-1}.

The $CdSe_{LO}$ mode in the as-deposited OAD films is broader and slightly red-shifted in the composite films compared to the pure CdSe film. After annealing, the Raman peak attributed to the $CdSe_{LO}$ mode sharpens for films $C^{33}T^{67}$, $C^{40}T^{60}$, and $C^{46}T^{54}$, while for films $C^{13}T^{87}$ and $C^{23}T^{77}$ this peak disappears. The intensity of the $CdSe_{LO}$ peak in the pure CdSe film annealed at $T = 400$ °C decreases slightly. Another peak, at $\Delta\nu \approx 152$ cm^{-1}, is seen in all of the as-deposited composite films but not in the pure CdSe film. This peak also disappears after annealing.

It is difficult to assign the peak at $\Delta\nu \approx 152$ cm^{-1}. While trigonal (t-Se), monoclinic (α-Se), and amorphous (a-Se) selenium are known to have Raman bands in the region from $\Delta\nu =$ 140–150 cm^{-1}, typically the most intense Se-related Raman bands occur in the region $\Delta\nu = 230$–270 cm^{-1},[48] and no distinct Raman peaks are observed in this region in our samples. CdSe, SeO_x, $TiSe_x$, and CdO do not have Raman bands near $\Delta\nu \approx 150$ cm^{-1}. Although the anatase and rutile phases of TiO_2 have Raman bands near $\Delta\nu \approx 150$ cm^{-1}, the observed peak is not related to a crystalline phase of TiO_2 because the as-deposited TiO_2 has been shown to be amorphous. Furthermore, the peak at $\Delta\nu \approx 152$ cm^{-1} disappears after annealing at $T = 400$ °C (Fig. 6), and a mode associated with crystalline TiO_2 would be expected to sharpen after the annealing treatment. A peak associated with the excess Se would be apparent in the as-deposited films and disappear in the annealed films as described above. Thus, the peak at $\Delta\nu \approx 152$ cm^{-1} is cautiously assigned to Se. In particular, this peak should be associated with how the Se is incorporated and interacts with the surrounding TiO_2 lattice because it is not apparent in the pure CdSe spectrum. According to Ren *et al.* it is possible that the A_1 and E_1 modes of helical Se chains found at $\Delta\nu = 257$ cm^{-1} and $\Delta\nu = 233$ cm^{-1}, respectively, can red-shift to $\Delta\nu \approx 150$ cm^{-1} and $\Delta\nu \approx 200$ cm^{-1}, respectively, when under hydrostatic pressure.[49] Helical chains of Se exhibit negative compressibility under hydrostatic pressure, which means that as the pressure increases the chain lengthens while the radius

decreases. It is possible that Se clusters embedded in the TiO_2 matrix undergo a similar process in which the *c*-axis elongates while the radial coordinates decrease, leading to the observed Raman spectral pattern of two peaks near $\Delta\nu \approx 150\ cm^{-1}$ and $\Delta\nu \approx 200\ cm^{-1}$ in the composite films.

The state of the CdSe within the composite structures changes after annealing at $T = 400\ ^\circ C$, and this change depends on the composition of the film. The $CdSe_{LO}$ peak sharpening in the $C^{33}T^{67}$, $C^{40}T^{60}$, and $C^{46}T^{54}$ films with annealing indicates an improvement in CdSe crystallinity in these films, which is consistent with the XRD results of the $C^{46}T^{54}$ film. The loss of the $CdSe_{LO}$ peak in the $C^{13}T^{87}$ and $C^{23}T^{77}$ films could result from alloying of the materials or CdSe domain size shrinkage so that they are beyond the detection limit. The latter is more probable given the lack of evidence of alloying in all of the other films. A decrease in the CdSe crystallite size could be the result of thermal oxidation.[50] The loss of CdSe through oxidation into CdO would be facilitated by the extremely short oxygen diffusion lengths in the highly porous OAD nanorod structure and the smaller expected crystallite sizes in the $C^{13}T^{87}$ and $C^{23}T^{77}$ films. It is also possible that the primary contribution to the Raman band at $\Delta\nu \approx 207\ cm^{-1}$ in the $C^{13}T^{87}$ and $C^{23}T^{77}$ films is from a red-shifted mode of Se (see discussion above), instead of the $CdSe_{LO}$ mode,[49] and that the loss of the mode in these films is related to the loss of Se instead of the loss of CdSe.

The Raman analysis shows that the way CdSe and Se is incorporated into the TiO_2 lattice changes with annealing, and that this change is dependent on the material composition and, therefore, on the material stoichiometry. The loss of the Raman bands associated with CdSe and Se in the annealed $C^{13}T^{87}$ and $C^{23}T^{77}$ OAD films demonstrates that isolated Se and $CdSe_{1-x}$ regions, as described in Fig. 5, are less stable within TiO_2 since these regions are initially more prevalent in these films. The $CdSe_{LO}$ Raman peak sharpening in the annealed $C^{33}T^{67}$, $C^{40}T^{60}$, and $C^{46}T^{54}$ films demonstrates that when $CdSe_{1-x}$ regions overlap with Se regions, which is more likely to occur in these films, CdSe domains within a TiO_2 matrix are stabilized and can improve in crystalline quality with annealing.

3.2 Optical properties of OAD films

The OAD CdSe–TiO_2 films were further characterized by UV-visible (UV-vis) spectroscopy. As seen in Fig. 7a, the as-deposited pure CdSe OAD film shows extensive visible light absorbance, while the pure TiO_2 film does not begin absorbing appreciably until the incident wavelength falls below 400 nm. The spectra of the composite as-deposited OAD films show a gradual transition between the pure samples, with the films having higher CdSe compositions absorbing more visible light. The only exception to this pattern is that the $C^{40}T^{60}$ film absorbs visible light more strongly than the $C^{46}T^{54}$ film. Thus, the absorbance spectra of the as-deposited films generally appear as one would expect for CdSe–TiO_2 films of varying composition.

Annealing at $T = 400\ ^\circ C$ greatly alters the optical properties of the OAD films. For the pure CdSe OAD film, the absorbance decreases slightly in the UV region but increases slightly in the visible region (Fig. 7b). The pure TiO_2 film shows an increase in absorbance for both the UV and near-UV regions after annealing, which is typical of OAD TiO_2 films. After annealing, the composite films show much less absorbance across the whole spectrum and no longer show a monotonic increase in visible light absorbance with increasing CdSe composition. Instead, the $C^{13}T^{87}$ film shows the greatest visible light absorbance, and the $C^{40}T^{60}$ film shows the least.

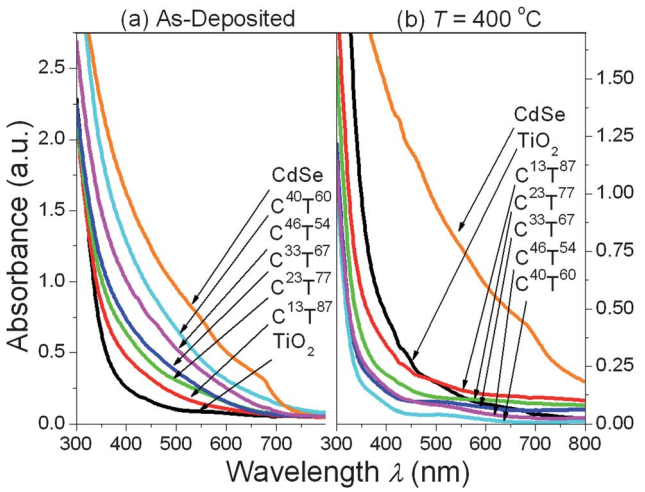

Fig. 7 UV-vis absorbance spectra of the (a) as-deposited and annealed (b) OAD films.

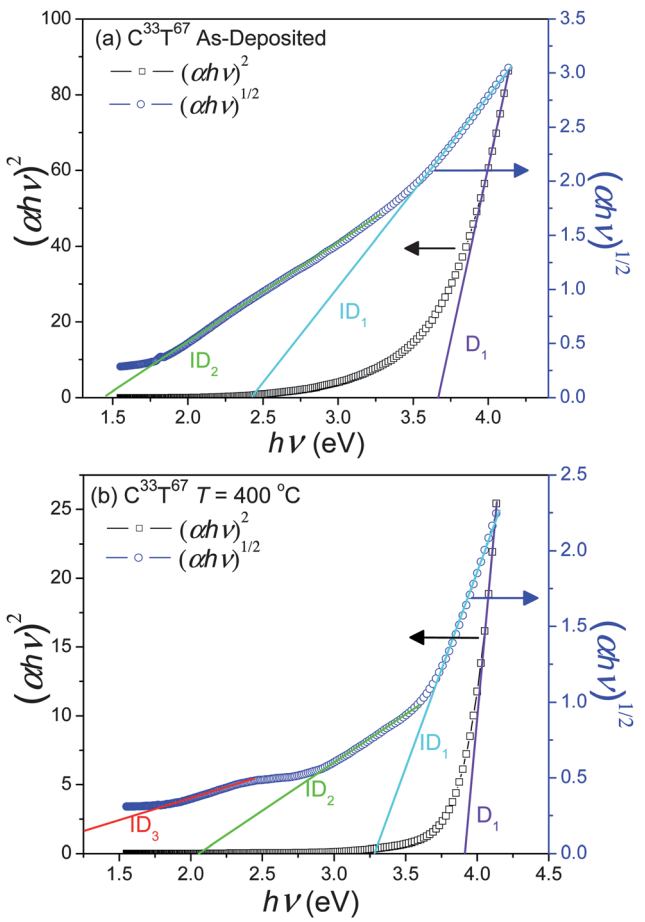

Fig. 8 Example Tauc plot extrapolations showing the spectra of the (a) as-deposited and (b) annealed $C^{33}T^{67}$ films.

A better understanding of the optical properties of the films is obtained by analyzing the optical transitions extrapolated from Tauc plots of the films. Examples of the Tauc plot fittings are shown in Fig. 8a and b, which show the plots for the OAD $C^{33}T^{67}$ as-deposited and $T = 400$ °C films, respectively. As can be seen in both of the Tauc plots, the curves that correspond with direct transitions, $(\alpha h\nu)^2$ *versus* $h\nu$, have only one linear region, while the curves corresponding with indirect transitions, $(\alpha h\nu)^{1/2}$ *versus* $h\nu$, exhibit more than one linear region. Thus, there is more than one optical transition occurring in each film. These transitions are labeled D_n for direct transitions and ID_n for indirect transitions, where n is an integer and the numbering scheme is such that the optical transition energy, E_g, decreases as the number increases. A summary of the optical transitions that have been extrapolated from the Tauc plot fittings of the composite and pure films is shown in Fig. 9. The results are consistent with the behavior seen in the absorbance spectra; the as-deposited films have optical transition energies that monotonically increase with decreasing CdSe composition, and annealing the OAD films at 400 °C increases the transition energies of the composite films and alters the simple monotonic behavior.

For the as-deposited pure TiO_2 film (Fig. 8a), $E_{D_1} = 3.7$ eV and $E_{ID_1} = 3.0$ eV, which agree reasonably well with the direct and indirect transitions of amorphous TiO_2 at 3.8 eV and 3.0 eV, respectively.[51] For the second indirect transition, ID_2 occurs at 1.7 eV and is attributed to oxygen vacancies in the oxygen-deficient as-deposited TiO_2 OAD film.[52] For the as-deposited pure CdSe film, $E_{D_1} = 3.4$ eV, which could be attributed to the excess Se in the film since indirect transitions in trigonal Se nanowires in the region from $E_g = 3.2$–3.4 eV have been described previously.[53] No quantum size effects are expected to occur for this polycrystalline film, so it is not likely that D_1 is associated with CdSe. $E_{ID_1} = 1.7$ eV in the pure CdSe film, which agrees well with the bulk band gap values of Se and CdSe. For the pure CdSe film, ID_2 appears at 1.11 eV and could be associated with a blue-shifted band of CdO.[54] In the as-deposited composite films, ID_1 can be considered an effective band gap since it is not possible to separate out the contributions from different transitions occurring in Se, CdSe, and TiO_2, so the extrapolated linear region is the result of the relative material composition of each film. As such, it varies approximately linearly from $E_{ID_1} = 2.1$–2.8 eV, increasing in energy with increasing TiO_2 composition. E_{ID_2} is in the range of 1.4–1.7 eV, increases as the TiO_2 composition increases, and is related to oxygen vacancies in the TiO_2 lattice. D_1 follows the same general trend as ID_2 and gradually varies from $E_{D_1} = 3.5$–3.7 eV, and is also attributed to transitions in TiO_2.

After annealing at $T = 400$ °C, the pure TiO_2 OAD film is in the anatase phase, and the corresponding change in the direct and indirect energy gaps is slight, with $E_{D_1} = 3.6$ eV and $E_{ID_1} = 3.0$ eV. The value of the indirect band gap is slightly lower than the bulk value of 3.2 eV, suggesting that not all of the oxygen vacancy defects have been passivated. The extrapolated band gap energies of the annealed pure CdSe OAD film change more significantly, with $E_{ID_1} = 0.8$ eV and $E_{D_1} = 2.8$ eV, where ID_1 corresponds with a low energy transition of CdO and D_1 corresponds with a convolution of transitions in CdSe and SeO_x.[55]

The optical transitions for the annealed composite films are more complicated. Both D_1 and ID_1 are respectively attributed to the direct and indirect transitions of TiO_2. However, both E_{ID_1} and E_{D_1} for the annealed films are blue-shifted relative to both the as-deposited E_g values and the bulk E_g values of amorphous, rutile, and anatase TiO_2. This is attributed to a Moss–Burstein shift resulting from the oxygen-deficient TiO_2 behaving as a degenerately doped semiconductor.[56] There are two lower energy transitions, ID_2 and ID_3, obtained for the annealed composite films. Both of these transitions are complicated functions of film composition. ID_3 is only discernible in the Tauc plots of the $C^{46}T^{54}$, $C^{40}T^{60}$, and $C^{33}T^{67}$ films, and is found at $E_{ID_3} = 1.3$ eV, $E_{ID_3} = 1.6$ eV, and $E_{ID_3} = 0.8$ eV, respectively. E_{ID_3} is widely varying, which is the result of varying contributions from several phases. The relatively lower energy of ID_3 indicates contributions from CdO and oxygen vacancies in TiO_2. Additionally, the incorporation of Se into the TiO_2 lattice to form TiO_2-Se would contribute to absorbance in this region by

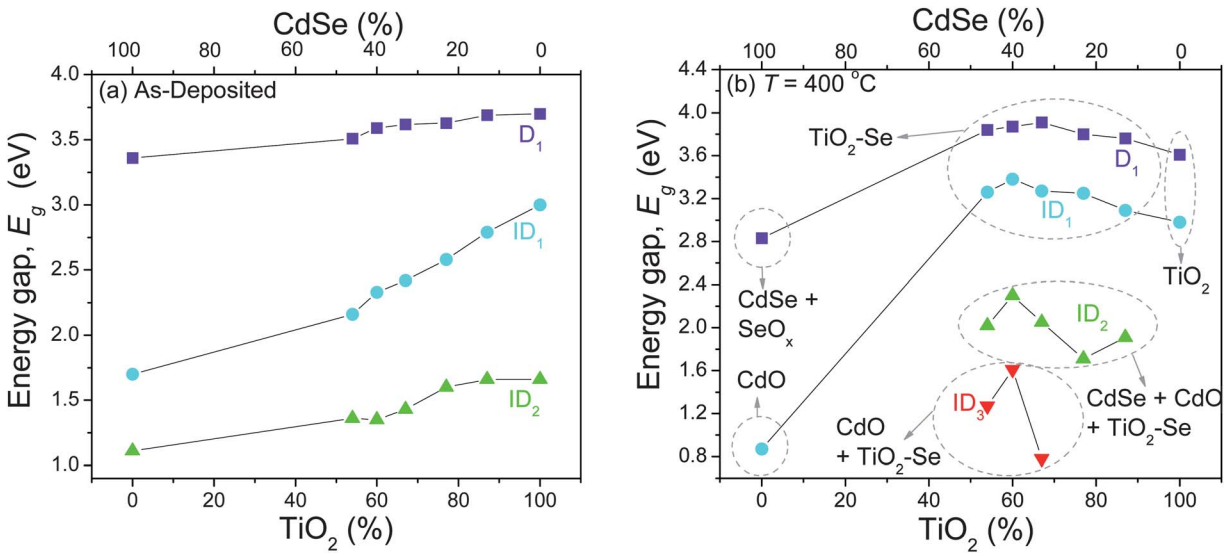

Fig. 9 Extrapolated energy gaps from the Tauc plots as a function of TiO_2 composition for the (a) as-deposited and (b) annealed OAD films. The gray circles indicate the transitions associated with a common phase, which is indicated by the arrow.

inducing several states within the forbidden gap of TiO_2[38] and by maintaining or increasing the oxygen deficiency of the TiO_2 lattice as indicated by the EDX analysis (Fig. 1). Similar to ID_3, ID_2 is widely varying, with $E_{ID_2} = 1.7–2.3$ eV, and is a complicated function of material composition. In addition to possible contributions from CdO and TiO_2-Se, the optical transitions of CdSe will play a role in ID_2, as well.

The increase in the number of observed optical transitions in the Tauc plot fittings of the annealed composite films is not due the emergence of a new optical transition, but rather to the loss of a strong optical transition that had previously obscured weaker ones in the as-deposited films. This is clearly seen in a decrease in the values of $(\alpha h\nu)^2$ and $(\alpha h\nu)^{1/2}$ *versus* $h\nu$ in the Tauc plots (Fig. 8) and also in the change in the absorbance spectra of the composite films (Fig. 7). This can also be seen by visual inspection, as the composite films change from a reddish-brown to mostly transparent after annealing (see ESI Fig. S3†). The brown hue is the result of CdO, while the red hue is attributed to Se.[57] Thus, the loss of the red color is the result of the disappearance of elemental Se and its associated optical transitions. While the excess Se is no longer present as elemental Se after annealing, the excess Se still affects the optical properties of the composite films be residing substitutionally in the TiO_2 lattice. The incorporation of Se into the TiO_2 lattice is seen by transitions in the Tauc plots, ID_1, ID_2, ID_3, and D_1, which are related to TiO_2-Se and oxygen-deficient TiO_2, where the non-stoichiometry is preserved by the substitutional Se.

3.3 Photoelectrochemical properties of OAD films

Two different electrochemical experiments were performed on both as-deposited and annealed the OAD CdSe–TiO_2 films, cyclic voltammetry and incident photon to current conversion efficiency (IPCE) measurements. Fig. 10 shows the photocurrent density measured for all of the films under white light illumination. Both the pure TiO_2 and pure CdSe OAD as-deposited films exhibit scant photocurrent density under white light illumination. After annealing at $T = 400$ °C, the measured photocurrent density increases for both pure films, with the annealed pure CdSe film showing a greater photocurrent than the annealed pure TiO_2 film. For the composite films, the opposite is true; the as-deposited composite films generally have a higher photocurrent density than the annealed composite films. The as-deposited and annealed composite films also exhibit opposite trends in measured photocurrent density with varying CdSe content. For the as-deposited samples, the films with smaller CdSe compositions outperform the films with higher CdSe compositions, and after annealing at $T = 400$ °C, the films with higher CdSe compositions outperform films with lower CdSe compositions. Notably, four different composite films, the as-deposited $C^{13}T^{87}$, as-deposited $C^{23}T^{77}$, as-deposited $C^{46}T^{54}$, and annealed $C^{46}T^{54}$ films, have a higher photocurrent density than the annealed pure TiO_2 film. And, one film, the as-deposited $C^{13}T^{87}$ film, has a higher visible light photocurrent density than the annealed pure CdSe film. This demonstrates that composite structures are, in some cases, more efficient photoelectrochemically than their single material counterparts.

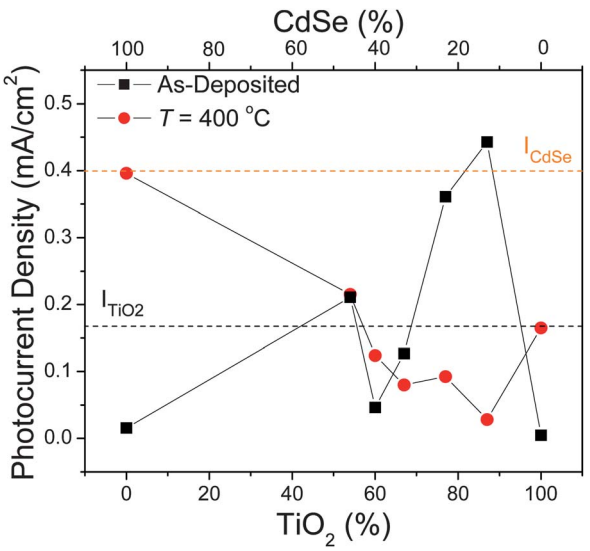

Fig. 10 Measured photocurrent density of the as-deposited and annealed OAD films as a function of composition.

The change in observed photocurrent density in the TiO_2 samples with annealing is straight-forward; poor crystalline quality and large band gap conspire to produce low photocurrent density in the as-deposited pure TiO_2, and annealing improves the crystalline quality of the film, increasing the measured photocurrent. The behavior for the pure CdSe is interesting. The crystalline quality of the pure CdSe film is expected to be better than that of the pure TiO_2 film since it has a well-defined X-ray diffraction pattern, and, additionally, the as-deposited CdSe showed significant visible light absorbance in its UV-vis spectrum. However, the difference in photocurrent between the as-deposited CdSe and TiO_2 is much smaller than expected given the better visible light absorbance and crystalline quality of the CdSe film, suggesting charge recombination is an important factor in the photoelectrochemical performance of the as-deposited pure CdSe film. The measured photocurrent of the CdSe film significantly improves after annealing at $T = 400$ °C, but this is not solely due to improved crystalline quality. As seen in the SEM images (Fig. 2), the excess Se in the annealed pure CdSe films melts out from the bulk of the nanorods to the exterior surfaces, where it can escape as vapor or reside as a surface SeO_x layer. Surface elemental Se in non-stoichiometric CdSe are known hole traps and have been shown to completely quench photoluminescence.[58] Thus, the movement of Se from the inter-granular spaces to the nanorod surface improves inter-granular charge transport and increases photocurrent density. The substantial improvement in CdSe photocurrent density after annealing highlights the deleterious effect of the inter-granular Se in the as-deposited film. It should be noted that the annealed pure CdSe OAD film did show unstable, fluctuating photocurrent. It is not clear why this behavior was observed, but it might be related to the reactions associated with photocorrosion in CdSe.[59]

The mechanisms determining the observed photocurrent density of the composite films are not as straight-forward. Thus, further analysis is necessary to elucidate the photoelectrochemical behavior of these films. It is worthwhile to note that while the nanostructured surface area can play an important role in PEC performance, it appears to play a relatively insignificant role in the measured photocurrent density of the OAD composite films. This can be observed by comparing the photocurrent densities of the as-deposited $C^{13}T^{87}$ and $C^{23}T^{77}$ films,

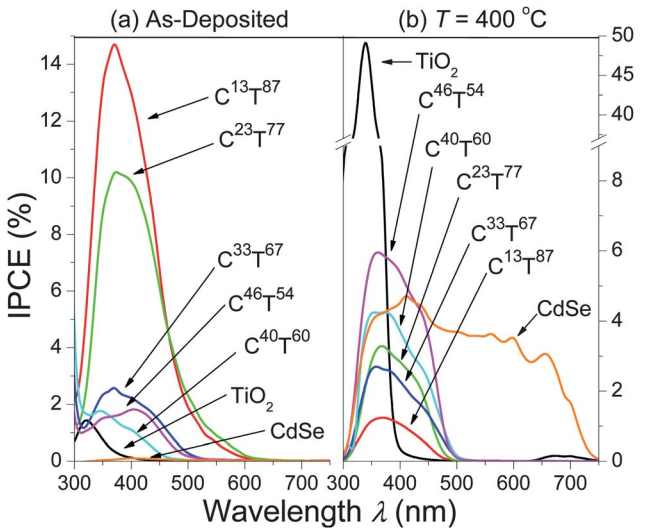

Fig. 11 Incident photon to current efficiency (IPCE) spectra for the (a) as-deposited and (b) OAD films annealed at $T = 400$ °C.

which have very different surface areas (Table 2) but similar photocurrent densities, and by comparing the photocurrent densities of the as-deposited $C^{13}T^{87}$ and $C^{46}T^{54}$ films, which have similar surface areas but very different photocurrent densities. This result is not surprising, as the majority of the surface area in the composite films is composed of the TiO_2 host, which has a mostly passive role under white light illumination.

In order to obtain a better understanding of the measured visible light photocurrent density and its spectral dependence, IPCE measurements were taken. As expected, the IPCE spectra (Fig. 11) exhibit the same general trends as the measured photocurrent density; films with a higher measured photocurrent show greater current conversion efficiency across the visible spectrum. For the pure films, the as-deposited IPCE spectra show very low conversion efficiency across the UV and visible regions. After annealing, the pure TiO_2 film shows efficient conversion beginning at $\lambda = 400$ nm, and the pure CdSe film shows relatively efficient conversion over the range $\lambda = 300$–750 nm. The spectra are more complicated for the composite films. The films have similar ranges of efficacy, $\lambda = 300$–600 nm for the as-deposited composites, and $\lambda = 300$–500 nm for the annealed composites. However, the shape and height of these curves over these ranges vary for different composite films.

Each IPCE spectrum shows a unique structure, and deconvoluting the spectra using Gaussian functions allows for a comparison of the electronic transitions generating photocurrent for each sample. Each spectrum was deconvoluted using the minimum number of Gaussian curves that could reproduce the measured spectrum with good fidelity (see ESI Fig. S4† for plots of the fittings). The lower energy edge of each Gaussian peak is considered that electronic transition's onset. The transitions that were deconvoluted for each film are plotted in Fig. 12a and b. It is important to note that it is difficult to make comparisons between the deconvoluted IPCE transitions and the Tauc plot extrapolated optical transitions described above; not all optically active transitions can generate a measurable photocurrent, and transitions which can generate a photocurrent may be hidden in the Tauc plots due to the multi-phase nature of the films.

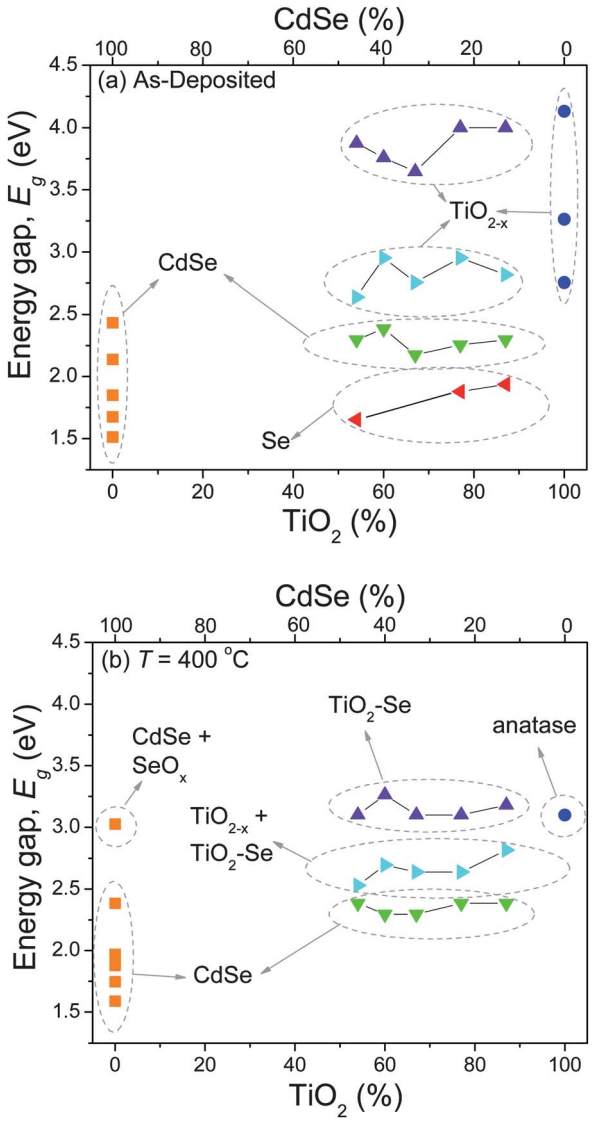

Fig. 12 Energy of the Gaussian transitions deconvoluted from the IPCE spectra of the OAD films, (a) as-deposited and (b) annealed at $T = 400$ °C. The gray circles indicate the transitions associated with a common phase, which is indicated by the arrow.

As shown in Fig. 12a, the Gaussian transitions extracted from the pure TiO_2 spectra are unsurprising, with the as-deposited film showing relatively inefficient transitions associated with amorphous, oxygen-deficient TiO_2, and the annealed film showing one efficient transition corresponding with the band gap of anatase TiO_2. The IPCE spectra of the as-deposited and annealed CdSe OAD films are described by very similar Gaussian peaks, with the one exception of the transition at $E_g \approx 3.0$ eV that appears in the annealed spectrum and could be related to the surface SeO_x layer. Thus, it is not specific transitions that determine the greater photocurrent generation in the annealed CdSe film. Instead, the annealing treatment improves the photon to electron conversion efficiency of the transitions that already occur in the as-deposited film. The improvement in efficiency in the annealed film is related to the segregation and oxidative passivation of the intergranular and surface Se, as described above.

The composite OAD films behave similarly as the pure CdSe film in that all the composite films generally exhibit the same electronic transitions; however, the efficiency of these transitions is greater in some films than in others. A notable exception is a low energy transition that is only seen in the as-deposited $C^{13}T^{87}$, $C^{23}T^{77}$, and $C^{46}T^{54}$ films and appears at 1.94 eV, 1.89 eV, and 1.65 eV, respectively (Fig. 12a). These particular films are among the films that generate the greatest photocurrent under visible light illumination. This low energy Gaussian peak has a relatively small height when compared to the other deconvoluted peaks (see ESI Fig. S4b, S4c and S4f†), which highlights how a relatively inefficient low energy transition can improve the photocurrent generation of TiO_2-based structures under visible light illumination. The loss of this transition with annealing indicates that it is associated with the excess Se. The observation that it appears only in the films that are most likely to have isolated Se clusters further strengthens this attribution.

The other deconvoluted transitions are associated with CdSe and TiO_2 phases, but the way in which each of these phases interacts with Se determines their conversion efficiency. An illustrative example is the behavior of the transition seen in the composite spectra that occurs in the $E_g = 2.2$–2.4 eV region; this transition is attributed to CdSe due to its appearance in the as-deposited and annealed pure CdSe IPCE spectra. Its energy value remains relatively constant across all samples, both before and after annealing, but the relative efficiency of this transition and how it changes with annealing is a function of film composition. In films with a greater CdSe composition the IPCE of this transition is relatively low, and annealing the films improves the conversion efficiency. The opposite is true for films with lower CdSe compositions; this transition has a greater IPCE in the as-deposited films than in the annealed films. This observed behavior can be explained by considering the structural properties of the films. As shown in Fig. 5, $CdSe_{1-x}$ domains are more likely to coincide with Se regions in the films with a greater CdSe composition, creating Se-rich CdSe clusters in these films. Similar to what occurs in the pure CdSe film, this excess Se prevents efficient charge transfer from CdSe domains to the TiO_2 matrix. Annealing the films incorporates the excess Se into the TiO_2 lattice, which improves charge transfer across the interface and increases the IPCE of this transition. This is clearly demonstrated in the photocurrent density of the $C^{46}T^{54}$ and $C^{40}T^{60}$ films (Fig. 10); their measured Cd + Se/(Cd + Se + Ti + O) ratios are very similar, but the $C^{40}T^{60}$ film is much more non-stoichiometric. The difference between the measured photocurrents of the two films decreases with annealing because the $C^{40}T^{60}$ film benefits more from the incorporation of the Se into the TiO_2 lattice due to its larger Se/Cd ratio in the as-deposited film. Thus, the IPCE associated with the CdSe transition improves with annealing for the films with greater CdSe content because the negative effects of the excess Se surrounding the CdSe domains are minimized once the Se becomes incorporated within the TiO_2 lattice. This is contrast with the films with lower CdSe content, where the IPCE of CdSe transitions decreases with annealing. This is because CdSe is more likely to be found in small, Se-deficient clusters in these films. The charge transfer from CdSe to TiO_2 is much more efficient in the as-deposited films with lower CdSe compositions because they lack the surface Se defects found in higher compositions. However, as described above, small Se-deficient clusters are more easily oxidized into CdO during the annealing treatment, while Se-rich CdSe clusters are more stable. This loss of CdSe in the films with lower CdSe content through oxidation during annealing is indicated by the disappearance of CdSe modes in the Raman spectra (Fig. 6). Thus, the decrease in the IPCE of the CdSe transitions for the films with lower CdSe compositions is due to the partial or complete oxidation of CdSe into CdO.

The appearance of CdO is not just deleterious to the IPCE and measured photocurrent density due to the physical loss of CdSe; it also acts as a recombination center. The two higher energy transitions in the as-deposited and annealed composite films (Fig. 12) are attributed to oxygen-deficient TiO_2 (TiO_{2-x}) and to both TiO_{2-x} and TiO_2-Se, respectively. These transitions mirror the behavior of the CdSe transition. Films with lower CdSe compositions show higher IPCE for the TiO_2-related transitions before annealing and lower IPCE after annealing, and films with higher CdSe compositions show lower IPCE among these transitions before annealing and higher IPCE after annealing. This is a surprising result, as one might expect that, after annealing, the films with the greatest material volumes of pure TiO_2 should have the greatest IPCE for TiO_2-related transitions. Instead, the opposite is true. This result is explained by the oxidation of the CdSe domains into CdO within the bulk of the nanorod, which, as described above, is more significant in the films with lower CdSe compositions. The negative effects of CdO on the charge transport properties of wide band gap semiconductors have been observed before.[60,61] The conduction and valence bands of CdO are bracketed by the conduction and valence bands of TiO_2. The CdO conduction band is more positive than the TiO_2 conduction band, and the CdO valence band is more negative than the TiO_2 valence band. Therefore, CdO domains within a TiO_2 matrix will trap both electrons and holes generated during the photoexcitation of TiO_2, and since both charge carriers are trapped in the same localized region, the CdO domains will act as recombination centers, reducing efficiency and photocurrent. Similarly, the CdO conduction band is more positive than the CdSe conduction band. Thus, photogenerated electrons from CdSe will be trapped by adjacent CdO regions increasing charge recombination and decreasing charge transfer efficiency across the interface into TiO_2. The effect of CdO recombination centers is not apparent in the films with greater CdSe composition. In agreement with the Raman data, this indicates that the Se-rich CdSe regions and the corresponding TiO_2-Se regions inhibit the formation of CdO during the annealing treatment.

4. Conclusions

In this work, it is determined that the two phase evaporation process of CdSe strongly governs the observed properties of CdSe–TiO_2 composites fabricated by oblique angle codeposition. In order to achieve smaller mol% of CdSe, lower evaporation rates of CdSe are necessary, but these lower rates favor the formation of isolated regions of Se and $CdSe_{1-x}$ within the film structures. Greater CdSe content entails higher evaporation rates of CdSe, which not only increases the amount of $CdSe_{1-x}$ relative to Se, but also increases the likelihood that these two regions will come in close proximity within the TiO_2 matrix. Thus, the relative prevalence of these three regions (Se, $CdSe_{1-x}$, and

overlap) varies for different material compositions. Furthermore, each of these regions has unique properties and is affected differently by the annealing treatment. The Se, $CdSe_{1-x}$, and overlap regions and their thermally induced phases (TiO_2-Se, CdO, c-CdSe, h-CdSe) interact differently with the TiO_2 matrix, which leads to the widely varying structural, optical and PEC properties of the composite films.

More importantly, this work demonstrates that oblique angle codeposition can be used to fabricate nanostructured, homogeneous composite photoanodes for PEC that are more efficient than non-composite structures of the same materials. Thus, the composite structure enhances the PEC properties compared to the constituent materials. In particular, the as-deposited $C^{13}T^{87}$ film generated a larger photocurrent under visible light illumination than the annealed pure CdSe film. Not only is this composite structure a more efficient visible light photoanode than the pure CdSe film, it is also more economically feasible and environmentally friendly to use than pure CdSe; the structure contains only ~8 mol% CdSe, an expensive and toxic semiconductor, and the rest of the structure is comprised of abundant, inexpensive, and non-toxic TiO_2. In addition, CdSe is known to have issues with photocorrosion. The stability of the measured photocurrent of the composite films was much improved over that of the pure CdSe film. Thus, composite films afford potential advantages over single material films.

Finally, the relatively large number of sample types considered in this work allows for the elucidation of general trends in the structural, optical, and PEC properties of CdSe–TiO_2 composite structures that are applicable toward the optimization of future nanostructure designs. Interestingly, the overall CdSe content within TiO_2 is a less critical parameter than the stoichiometry of the CdSe in determining the properties of the composite and how the material is affected during annealing. Se-deficient CdSe clusters within an oxygen-deficient TiO_2 matrix show effective charge-transfer across interfaces; however, small Se-deficient clusters are easily oxidized into CdO in the porous nanorods structure during open-air annealing. Se-rich CdSe clusters show less efficient charge-transfer but greater stability within the TiO_2 matrix during annealing. An optimal design should have a minimal CdSe content, where the CdSe has enough excess Se such that the clusters are stable enough that the film can be annealed to achieve a crystalline phase of TiO_2. However, this excess Se should not be so great as to prevent efficient charge-transfer across the CdSe–TiO_2 interface. Additionally, the optimized design will need to take into account the active role that the stoichiometry of the surrounding TiO_2 matrix has in determining the location of the excess Se atoms and the stability of the CdSe clusters during thermal treatment.

Acknowledgements

This work was supported by a DOE Hydrogen Initiative Award (DE-FG02-05ER46232). C. Longo was supported by the CAPES Visiting Fulbright Scholar Program.

References

1 A. Fujishima, *Nature*, 1972, **238**, 37–38.
2 K. Kalyanasundaram and M. Graetzel, *Curr. Opin. Biotechnol.*, 2010, **21**, 298–310.
3 S. U. M. Khan, M. Al-Shahry and W. B. Ingler, *Science*, 2002, **297**, 2243–2245.
4 C. Burda, X. Chen, R. Narayanan and M. A. El-Sayed, *Chem. Rev.*, 2005, **105**, 1025–1102.
5 P. V. Kamat, *J. Phys. Chem. C*, 2007, **111**, 2834–2860.
6 A. Di Paola, G. Marcì, L. Palmisano, M. Schiavello, K. Uosaki, S. Ikeda and B. Ohtani, *J. Phys. Chem. B*, 2001, **106**, 637–645.
7 T. Umebayashi, T. Yamaki, H. Itoh and K. Asai, *J. Phys. Chem. Solids*, 2002, **63**, 1909–1920.
8 C. Burda, Y. Lou, X. Chen, A. C. S. Samia, J. Stout and J. L. Gole, *Nano Lett.*, 2003, **3**, 1049–1051.
9 W. Smith and Y. Zhao, *J. Phys. Chem. C*, 2008, **112**, 19635–19641.
10 W. Smith and Y. P. Zhao, *Catal. Commun.*, 2009, **10**, 1117–1121.
11 Y.-L. Lee and Y.-S. Lo, *Adv. Funct. Mater.*, 2009, **19**, 604–609.
12 D. Liu and P. V. Kamat, *J. Phys. Chem.*, 1993, **97**, 10769–10773.
13 I. Robel, V. Subramanian, M. Kuno and P. V. Kamat, *J. Am. Chem. Soc.*, 2006, **128**, 2385–2393.
14 J. H. Bang and P. V. Kamat, *Adv. Funct. Mater.*, 2010, **20**, 1970–1976.
15 J. Hensel, G. Wang, Y. Li and J. Z. Zhang, *Nano Lett.*, 2010, **10**, 478–483.
16 J. Kim, S. Choi, J. Noh, S. Yoon, S. Lee, T. Noh, A. J. Frank and K. Hong, *Langmuir*, 2009, **25**, 5348–5351.
17 W. Lee, S. H. Kang, S. K. Min, Y.-E. Sung and S.-H. Han, *Electrochem. Commun.*, 2008, **10**, 1579–1582.
18 T. Z. Markus, S. Itzhakov, Y. I. Alkotzer, D. Cahen, G. Hodes, D. Oron and R. Naaman, *J. Phys. Chem. C*, 2011, **115**, 13236–13241.
19 L.-W. Chong, H.-T. Chien and Y.-L. Lee, *J. Power Sources*, 2010, **195**, 5109–5113.
20 A. Kongkanand, K. Tvrdy, K. Takechi, M. Kuno and P. V. Kamat, *J. Am. Chem. Soc.*, 2008, **130**, 4007–4015.
21 J. B. Sambur, S. C. Riha, D. Choi and B. A. Parkinson, *Langmuir*, 2010, **26**, 4839–4847.
22 L. Liu, J. Hensel, R. C. Fitzmorris, Y. Li and J. Z. Zhang, *J. Phys. Chem. Lett.*, 2009, **1**, 155–160.
23 N. S. Guijarro, T. Lana-Villarreal, I. Mora-Seró, J. Bisquert and R. Gómez, *J. Phys. Chem. C*, 2009, **113**, 4208–4214.
24 Y. He, Y. Zhao and J. Wu, *Appl. Phys. Lett.*, 2008, **92**, 063107.
25 Y. He, J. Fan and Y. Zhao, *Cryst. Growth Des.*, 2010, **10**, 4954–4958.
26 Y. He, Z. Zhang, C. Hoffmann and Y. Zhao, *Adv. Funct. Mater.*, 2008, **18**, 1676–1684.
27 G. K. Larsen, R. Fitzmorris, J. Z. Zhang and Y. Zhao, *J. Phys. Chem. C*, 2011, **115**, 16892–16903.
28 Y. He, B. Yang, K. Yang, C. Brown, R. Ramasamy, H. Wang, C. Lundgren and Y. Zhao, *J. Mater. Chem.*, 2012, **22**, 8294–8303.
29 K. Robbie and M. J. Brett, *J. Vac. Sci. Technol., A*, 1997, **15**, 1460–1465.
30 Y. P. Zhao, D. X. Ye, G. C. Wang and T. M. Lu, *Nano Lett.*, 2002, **2**, 351–354.
31 B. C. Fitzmorris, G. K. Larsen, D. A. Wheeler, Y. Zhao and J. Z. Zhang, *J. Phys. Chem. C*, 2012, **116**, 5033–5041.
32 Y. He and Y. Zhao, *Nanoscale*, 2011, **3**, 2361–2375.
33 A. G. Sigai and H. Wiedemeier, *J. Electrochem. Soc.*, 1972, **119**, 910–914.
34 T.-S. Yang, C.-B. Shiu and M.-S. Wong, *Surf. Sci.*, 2004, **548**, 75–82.
35 Y. Zhao, Y. He and C. Brown, *Appl. Phys. Lett.*, 2012, **100**, 033103–033106.
36 S. Lichter and J. Chen, *Phys. Rev. Lett.*, 1986, **56**, 1396.
37 M. F. Kotkata, A. E. Masoud, M. B. Mohamed and E. A. Mahmoud, *Phys. E.*, 2009, **41**, 640–645.
38 J. W. Zheng, A. Bhattcahrayya, P. Wu, Z. Chen, J. Highfield, Z. Dong and R. Xu, *J. Phys. Chem. C*, 2010, **114**, 7063–7069.
39 J.-P. Ge, Y.-D. Li and G.-Q. Yang, *Chem. Commun.*, 2002, 1826–1827.
40 M. Epifani, E. Pellicer, J. Arbiol, N. Sergent, T. Pagnier and J. R. Morante, *Langmuir*, 2008, **24**, 11182–11188.
41 G. J. Fan, F. Q. Guo, Z. Q. Hu, M. X. Quan and K. Lu, *Phys. Rev. B: Condens. Matter*, 1997, **55**, 11010.
42 N. Suthan Kissinger, M. Jayachandran, K. Perumal and C. Sanjeevi Raja, *Bull. Mater. Sci.*, 2007, **30**, 547–551.
43 M. E. Rincón, A. Jiménez, A. Orihuela and G. Martínez, *Sol. Energy Mater. Sol. Cells*, 2001, **70**, 163–173.
44 O. Calzadilla, M. Zapata-Torres, L. Narvaez, S. Jiménez and F. Rábago, *Superficies y Vacio*, 2002, **14**, 35–37.
45 D. P. Masson, D. J. Lockwood and M. J. Graham, *J. Appl. Phys.*, 1997, **82**, 1632–1639.

46 L. E. Depero, *J. Solid State Chem.*, 1993, **104**, 470–475.
47 L. Daweritz, *J. Cryst. Growth*, 1974, **23**, 307–312.
48 G. Lucovsky, A. Mooradian, W. Taylor, G. B. Wright and R. C. Keezer, *Solid State Commun.*, 1967, **5**, 113–117.
49 W. Ren, J. T. Ye, W. Shi, Z. K. Tang, C. Chan and P. Sheng, *New J. Phys.*, 2009, **11**, 103014.
50 L. Liu, Q. Peng and Y. Li, *Inorg. Chem.*, 2008, **47**, 3182–3187.
51 V. Naik, D. Haddad, R. Naik, J. Benci and G. Auner, in *APS Meeting Abstracts*, Cambridge Univ Press, 2002.
52 N. Serpone, *J. Phys. Chem. B*, 2006, **110**, 24287–24293.
53 B. Gates, B. Mayers, B. Cattle and Y. Xia, *Adv. Funct. Mater.*, 2002, **12**, 219.
54 H. Köhler, *Solid State Commun.*, 1972, **11**, 1687–1690.
55 K. Tripathi, M. Husain and M. Zulfequar, *Chalcogenide Lett.*, 2009, **6**, 517–522.
56 E. Burstein, *Phys. Rev.*, 1954, **93**, 632–633.
57 R. Henriquez, P. Grez, E. Munoz, H. Gomez, J. Badan, R. Marotti and E. Dalchiele, *Thin Solid Films*, 2010, **518**, 1774–1778.
58 J. Jasieniak and P. Mulvaney, *J. Am. Chem. Soc.*, 2007, **129**, 2841–2848.
59 P. Allongue and R. Tenne, *J. Electrochem. Soc.*, 1991, **138**, 261.
60 R. Suárez-Parra, I. Hernández-Pérez, M. E. Rincón, S. López-Ayala and M. C. Roldán-Ahumada, *Sol. Energy Mater. Sol. Cells*, 2003, **76**, 189–199.
61 M.-H. Kim and Y.-U. Kwon, *J. Phys. Chem. C*, 2009, **113**, 17176–17182.